

Analysis of Resolution as a Function of Microparticle Size in Virtual Super-Resolution Optical Imaging for 2D System

A. R. Bekirov, Z. Wang, N. A. Lysceva, B. S. Luk'yanchuk, and A. A. Fedyanin
Lomonosov Moscow State University
bekirov@nanolab.phys.msu.ru

Abstract

The work shows that visualization using microparticles allows one to distinguish objects that are inaccessible during direct observation. This analysis is based on a full two-dimensional simulation of optical image formation taking into account the diffraction of partially coherent light on the microparticle and the objects under study. The oscillating nature of optical resolution is shown depending on the size of the microparticle. The presence of strong resonances is shown in both transmission and reflection modes.

1. Introduction

It was shown [1] that by examining objects with the help of dielectric microparticles, one can resolve structures beyond the diffraction limit. Various theoretical approaches have been proposed to explain this phenomenon [2-14]. These works are dedicated to modeling the super-resolution effect in virtual imaging by dielectric microspheres. Among them, some works focus on fully modeling the propagation of radiation from a source through the microsphere to the subsequent image formation [9, 10, 14]. In these models, the objects being imaged are not point dipoles but real structures. Due to computational complexity, such calculations are typically limited to two-dimensional cases. Experimental data confirmed super resolution effect for this case [15]. However, the crucial question of whether a fundamental resolution limit exists remains unresolved. This section examines the minimum achievable resolution in virtual imaging formed by microspheres and its dependence on particle size. Both reflection and transmission geometries are considered.

To investigate this issue, it is practical to use a monochromatic light source. To determine the system's resolution, a series of simulations must be conducted by gradually increasing the distance between the objects, starting from zero, until they become distinguishable in the image. The resolution criterion adopted is based on the Rayleigh criterion: first, the presence of two distinct intensity maxima in the image field; second, the intensity "dip" between the maxima must be 80% of the maximum intensity. It should be noted that some studies relax the second condition, requiring a dip of 95% or more. However, the 80% criterion provides a more reliable estimate of resolution for experimental validation.

In our previous work [14], we proposed a simulation method based on the FDTD (Finite Difference Time Domain) approach, which demonstrated its feasibility. However, this method is computationally intensive. For a monochromatic light source, the FEM (Finite Element Method) is more efficient and accurate. While the choice of method is less critical for fixed geometry simulations, the FEM approach becomes significantly advantageous when determining the resolution limit. Therefore, the calculations in this section are performed using the FEM method implemented in the Matlab Partial Differential Equation Toolbox, utilizing the specialized "electromagnetic" class of the "harmonic" type.

The structure of this paper is as follows: Section 2 examines various approaches to calculating the image field in the two-dimensional case for a spatially coherent source. Section 3 describes the calculation scheme. Section 4 discusses the method for computing the image for a spatially incoherent source and presents the conditions for resolving two objects in the image.

Section 5 presents the results of the study on the dependence of optical resolution on the particle radius, discusses certain specific features, and provides a comparison with the model of incoherent point sources.

2. Image field calculation approaches

There are several methods in the literature for calculating the image field at micrometer scales. In this section, we briefly describe them for the two-dimensional case. Let the field \mathbf{E} be generated by a certain coherent monochromatic source, which we will refer to as the source field. In this case, the temporal dependence takes the form $\sim e^{-i\omega t}$, which we will omit unless stated otherwise. The source field can be associated with its corresponding image field \mathbf{E}^{im} according to the following formula:

$$\mathbf{E}^{im}(r_0) = \frac{-i}{4} \int_{\Gamma} [G(\mathbf{n}, \nabla) \mathbf{E}^* - \mathbf{E}^*(\mathbf{n}, \nabla) G] dl, \quad (1)$$

where Γ is an arbitrary curve homotopic to an infinite line, $G = H_0^{(1)}(k|r - r_0|)$ is the Hankel function of the first kind, and $*$ denotes complex conjugation, $k = 2\pi/\lambda$, $\nabla = \partial / \partial \mathbf{r}$, λ is wavelength. The complex conjugation of the source field reverses the wave front, transforming the field from diverging to converging to the source.

Equation (1) can be rewritten in Fourier space as follows:

$$\mathbf{E}^{im}(r_0) = \frac{1}{2\pi k} \int_{-k}^k \tilde{\mathbf{E}}(k_x, y_0) e^{-i(k_x x - k_y(y - y_0))} dk_x, \quad (2)$$

where $\tilde{\mathbf{E}}$ is the Fourier transform of the field \mathbf{E} at $y = y_0$, and $k_y = \sqrt{k^2 - k_x^2}$. According to Eq. (2) and in accordance with Abbe's definition, the image field does not contain evanescent harmonics with $k_y > k$.

In the case where the source field is generated by scattering on a microparticle, the fields \mathbf{E}^{im} and \mathbf{E} can be expanded in terms of cylindrical functions. For the TM geometry ($E_x = E_y = 0$), these expansions take the following form [16]:

$$\begin{aligned} \mathbf{E} &= \sum_{l=-\infty}^{\infty} a_l \mathbf{N}_l, \\ \mathbf{E}^{im} &= \sum_{l=-\infty}^{\infty} a_l^{im} \text{Rg} \mathbf{N}_l^*. \end{aligned} \quad (3)$$

For convenience, the field \mathbf{E}^{im} is expanded using complex-conjugate functions, $\mathbf{N}_l = e^{il\varphi} H_l^{(1)}(k\rho) \mathbf{e}_z$, $H_l^{(1)}$ is the Hankel function of the first kind, and Rg denotes the extraction of the regular part of the expression. Due to the linearity of transformations (1)–(2), the column vectors of the expansion coefficients of the source field (a_l) and the image field (a_l^{im}) can be related by a matrix equation of the form:

$$\begin{pmatrix} \dots \\ a_{-1}^{im} \\ a_0^{im} \\ a_1^{im} \\ \dots \end{pmatrix} = \mathbf{A}^{im} \begin{pmatrix} \dots \\ a_{-1}^* \\ a_0^* \\ a_1^* \\ \dots \end{pmatrix}. \quad (4)$$

The components of the matrix \mathbf{A}^{im} are given by $(\mathbf{A}^{im})_{nm} = \text{sinc}((n-m)/2)$. This operator was first computed for the three-dimensional case in [12]. In the two-dimensional case, the calculations are analogous; for more details, see the Appendix.

For the TE geometry ($E_z = 0$), the fields \mathbf{E} and \mathbf{E}^{im} can be similarly expanded using functions $\mathbf{M} = \text{rot}(\mathbf{N})/k$. Due to the linearity of this transformation, Equation (4) and the components of the matrix A^{im} remain unchanged.

If the source field is non-stationary, $\mathbf{E} = \mathbf{E}(t)$, there are two approaches to computing the corresponding time dependence of $\mathbf{E}^{im}(t)$.

In the first approach, the time dependence can be expanded into a Fourier series. Then, by applying transformations (1)–(2) to each component and performing an inverse Fourier transform, the dependence $\mathbf{E}^{im}(t)$ can be obtained.

The second approach involves using the FDTD (Finite-Difference Time-Domain) method [14]. In this method, the field sources are explicitly defined at the grid nodes, and the field propagation in space is computed using a finite-difference scheme in the time domain. To ensure that the generated pulse corresponds to the image field rather than the source field, the time dependence must be reversed.

For the TM geometry, the setup of sources for generating the image field is implemented as follows:

$$E_z^{im}(x, y = y_o, t + dt) = E_z^{im}(x, y = y_o, t) + (E_z(x, y = y_o + dy, -t) - E_z(x, y = y_o, -t)) / dy + E_z(x, y = y_o, -t) / dy, \quad (5)$$

$$E_z^{im}(x, y = y_o + dy, t + dt) = E_z^{im}(x, y = y_o + dy, t) - E_z(x, y = y_o, -t) / dy, \quad (6)$$

where $y=y_0$ is the line on which the sources are defined, and dt, dy are the time and spatial grid steps, respectively. A similar approach can be applied in the TM geometry for each component E_x, E_y or by defining the source through the magnetic component H_z .

In our calculations, we used the FEM method, which allows us to obtain the spatial distribution of the source field. For this reason, we applied Equation (1). The curve Γ was chosen as a smooth, bell-shaped contour enclosing both the particle and the surrounding space. This configuration captures all rays emanating from the microsphere. If Γ were chosen as a straight line, achieving the same result would require the line to be significantly larger than the microsphere's diameter, substantially increasing the simulation domain. Similar optimizations were performed in Ref. [9].

3. Calculation Setup

For accurate calculations, the mesh size in the source generation and object regions must be especially fine. The maximum distance between mesh nodes was set to **0.066 λ** , with further refinement in the specified regions to 0.005λ . Simulations were conducted for microsphere sizes $R=(4:0.05:5)\lambda$ with a refractive index of $n=1.46$.

In the reflection geometry, the sample consisted of rectangular perfect conductors with a width of 0.25λ and a height of 0.1λ . For the transmission geometry, the sample was represented by slits in an opaque screen of the same dimensions. The entire structure was placed on a substrate with a refractive index of $n=1.46$.

The dimensions of the simulated region were $(2.2R+4\lambda) \times (2R+5.9\lambda)$. If the contact point between the microparticle and the substrate is taken as the origin, the curve Γ is defined by the following equation:

$$y = 3\lambda + (2R + 0.2\lambda) \left(1 + \left(\frac{x}{1.2R} \right)^4 \right)^{-1}$$

This dependence ensures a 3λ offset from the substrate surface to avoid edge effects. The overview of the calculation setup is shown in **Fig. 1**.

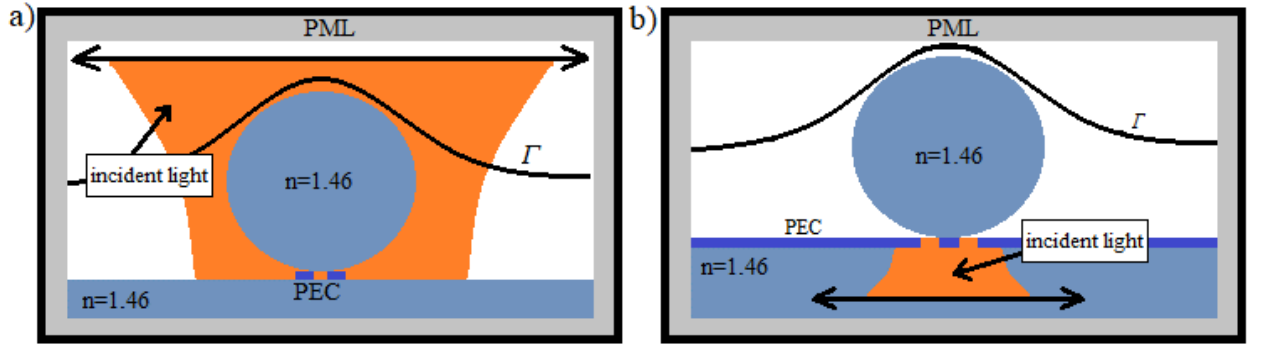


Fig. 1. General calculation scheme (not to scale): (a) reflection mode, (b) transmission mode.

To ensure a physically accurate assessment of the resolution, it is crucial to properly define the illumination conditions. In our calculations, we used two illumination schemes: the critical illumination scheme, where the image of an incoherent source is projected onto the sample, and the Köhler illumination scheme, where the sample is illuminated by incoherent plane waves at various angles.

In the critical illumination scheme, the calculation is performed for individual beams focused to a half-wavelength spot, with the focal point gradually shifted along the sample surface. The resulting intensities are then summed. The focal shift area depends on the visualization mode.

For the reflection mode, this area must exceed the size of the microsphere to ensure that further increasing the beam's spread does not alter the final image. In our calculations, this area ranged from $-1.7R$ to $1.7R$, where R is the radius of the investigated particle.

For the transmission geometry, light passes only through the limited area of the apertures, so it is sufficient to simulate beams focused on the aperture region rather than the entire particle size. In these calculations, the focal shift area ranged from -2λ to 2λ . However, the step size of the focal shift must be particularly small and is determined by the characteristic size of the apertures. According to this scheme, the coherence radius in the substrate plane equals $\lambda/2$.

In the Köhler illumination scheme, the sample is illuminated by plane waves within a cone with a half-angle of $3\pi/8$, with an angular step of $\pi/100$, in both transmission and reflection geometries.

Fig. 2 shows the near-field and the corresponding image field in the absence of a microparticle at different object distances for critical scheme illumination.

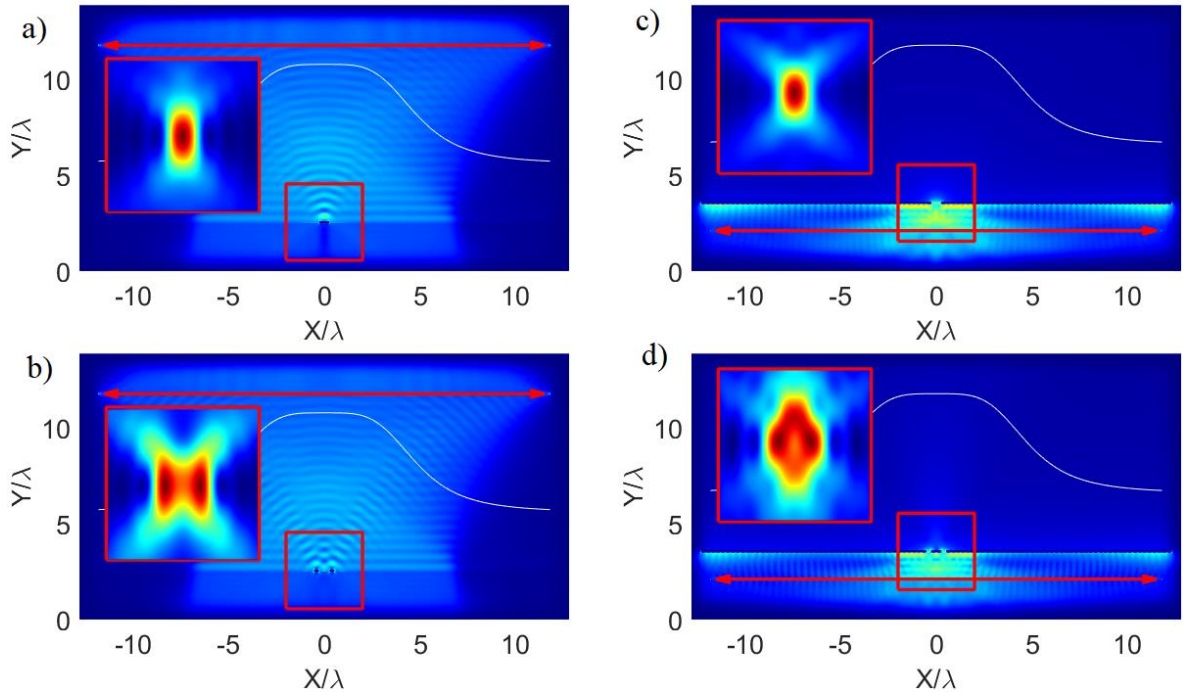


Fig. 2. Real fields without a microsphere and the corresponding image fields are shown in the insets. The white line represents the integration path Γ , the red double arrow line represents source injection line. The insets display the image field calculated for the area highlighted by the red square. (a, b) – Reflection mode, with distances between objects $d=0$ and $d=0.56\lambda$, respectively. (c, d) – Transmission mode, with distances between apertures $d=0$ and $d=0.54\lambda$, respectively. The results are obtained for the critical illumination scheme.

4. Image formation algorithm by incoherent source and criterion of the resolution

The algorithm for calculating the image field for a spatially incoherent source includes the following key steps:

1. Calculation of the image field for a given type of incident radiation: a beam focused on the sample surface for the critical illumination scheme and a plane wave with a specified incidence angle for the Köhler scheme.
2. Shifting the focal point along the substrate surface or changing the incidence angle for the critical and Köhler schemes, respectively.
3. Summation of intensity contributions from each focal point or incidence angle.

The image field is computed using Eq. (1) in a rectangular area centered at the geometric image position, determined by the magnification formula $n/(2-n)R$, with dimensions $(2.2R+4)\times 2R$.

The resolution condition is defined as follows: let the maximum of the image intensity field distribution for $x>0$ be at point A_1 , and for $x<0$ at point A_2 . The objects are considered **resolvable** if the intensity at the midpoint A_{12} exhibits an **80% dip** relative to the maxima at A_1 and A_2 .

In many cases, due to overlapping image fields from each object, the maximum shifts toward the center, forming a single peak above or below two distinct local maxima. If this central maximum is excluded, the resolution criterion is satisfied, and the objects (e.g., slits) can be considered resolvable. However, such cases are not considered in the presented calculations, meaning that the optical resolution is estimated conservatively, or “from below”.

Fig. 3 shows the near-field and the corresponding image field for a microparticle with $R=4.495\lambda$ at different object distances for critical scheme illumination.

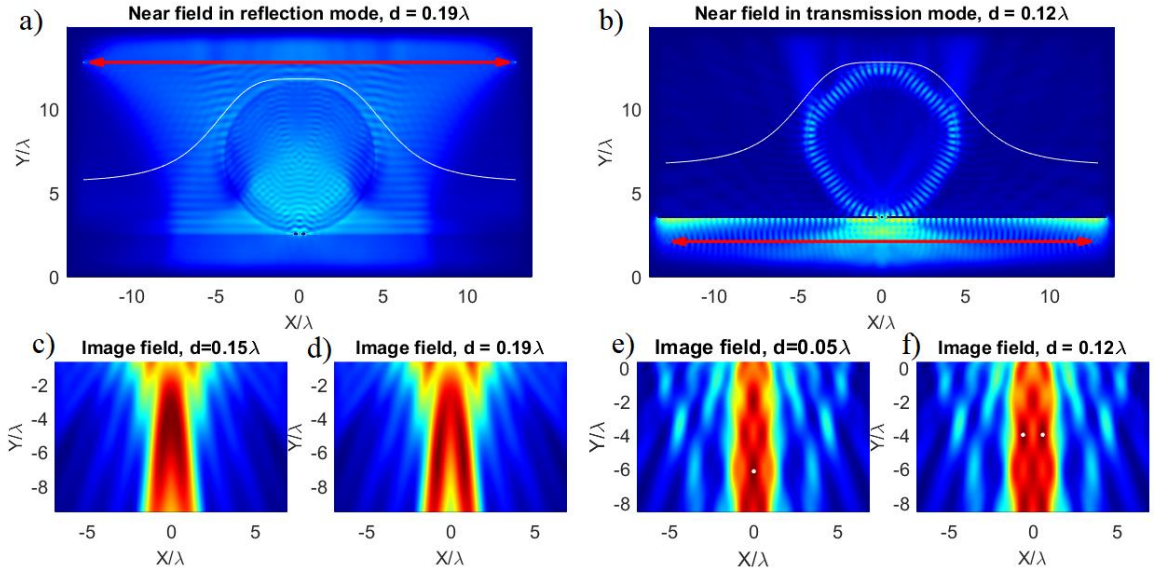


Fig. 3. (a, b) Near-field distribution in reflection and transmission modes for critical scheme illumination, respectively. Image field in reflection mode with object separation of $d=0.15\lambda$ – (c), $d=0.19\lambda$ – (d). Image field in transmission mode with slit separation of $d=0.05\lambda$ – (e), $d=0.12\lambda$ – (f). The white dots in (e)–(f) indicate the maximum field. The particle radius is $R=4.495\lambda$, $n = 1.46$. The white line represents the integration path Γ , the red double arrow line represents source injection line.

It should be emphasized that the microparticle does not generate an image in the same manner as in free space. In the case of a microsphere, the image appears as **elongated bright stripes**, whereas in free space, the image is localized on a wavelength scale, as evident from the comparison between **Fig. 2** and **Fig. 3**.

5. Results

To determine the optical resolution, we performed a series of calculations for a fixed particle radius while varying the distance between objects. The resolution was determined using the classical bisection method:

1. We define the lower and upper resolution bounds as distances S_1 and S_2 , where the objects are unresolved and resolved, respectively. By default, the resolution is assumed to be S_2 .
2. Next, we check whether the objects are distinguishable at the midpoint distance $S_{12} = (S_1 + S_2)/2$. If the objects are resolvable, we update the upper bound to $S_2 = S_{12}$; otherwise, we set the lower bound to $S_1 = S_{12}$.
3. We repeat step 2 until the difference between the upper and lower bounds becomes smaller than the predefined accuracy, $(S_2 - S_1) < \text{accuracy}$. We set the **accuracy** to **0.01**.

As the initial values, we set $S_1=0$ and $S_2=0.3\lambda$. If the objects remain unresolved at $S_2=0.3\lambda$, the upper bound is increased by 0.1λ until the objects become distinguishable.

In some cases, the resolution condition are satisfied even with zero separation ($S_1=0$), indicating that the sphere does not form an image that defines the object's geometry. In such cases, the resolution is considered indeterminate. These cases will be discussed in more detail later.

In **Fig. 4**, the graph illustrates the dependence of optical resolution on the size of the microparticle in transmission mode (TM) and reflection mode (RM). To visualize the resonance peaks, we added more calculation points for the reflection mode under critical illumination, while in all other cases, the calculation grid remained standard $R=(4:0.05:5)\lambda$. Fig. 4 also shows the resolution in free space, which slightly differs from $\lambda/2$ and is approximately 0.55λ . This can be explained by two factors: (a) the objects are not point sources, and (b) the coherence radius is not zero.

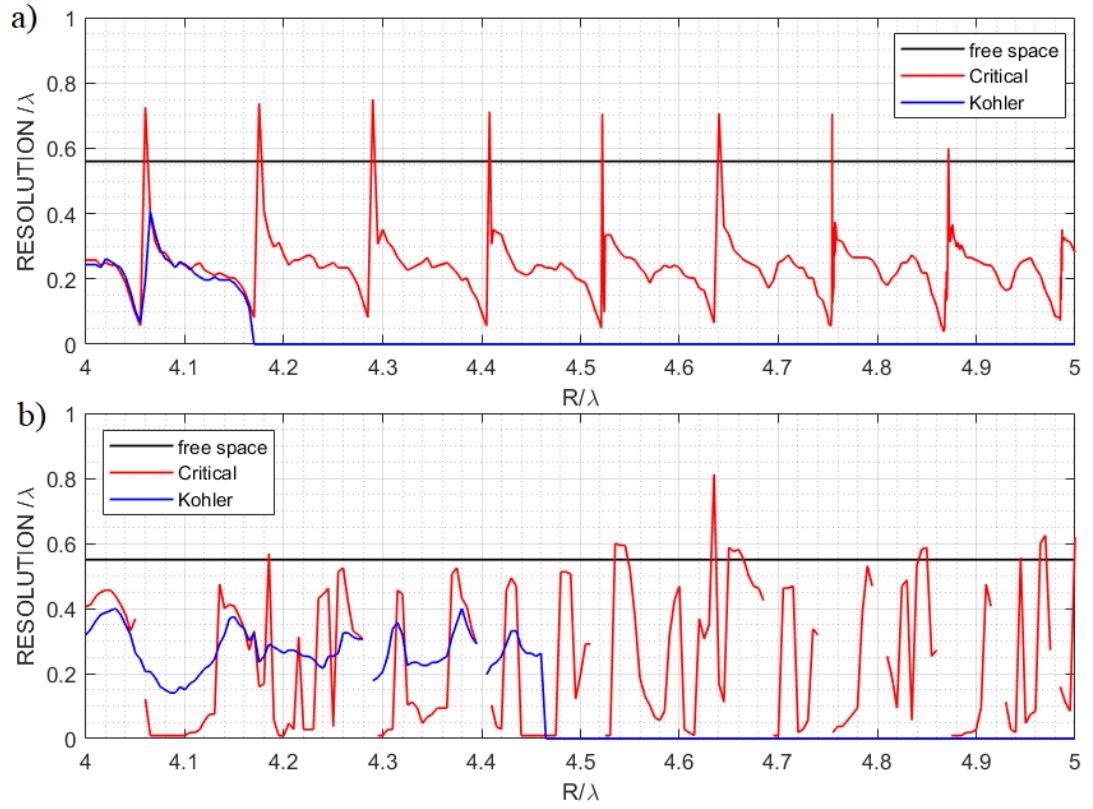


Fig. 4. Dependence of the optical resolution in the virtual image on the size of the microparticle: reflection mode - (a), transmission mode - (b). The black solid lines indicate the resolution in free space without the microparticle. At the discontinuity points in the graph for the transmission mode, the resolution is undefined because the slits are distinguishable (i.e., the resolution condition is satisfied) at zero distance. The resolution in free space for the critical illumination scheme and Köhler's scheme matches within the error margin (0.01), 0.55 and 0.56 for the transmission mode, and 0.55 and 0.56 for the reflection mode. To visualize the resonance peaks, more calculation points were added for the reflection mode under critical illumination (a). (Will be updated upon further calculation)

The calculations showed that the resolution in free space, i.e., in the real image, is approximately the same for both reflection and transmission geometries. However, for the virtual image, i.e., when a microparticle is present, it differs significantly. For the most cases, the optical resolution surpasses the free-space limit.

The graphs exhibit two types of distinctive features: in **Fig. 4(a)**, there are points of sharp resolution changes, while in **Fig. 4(b)**, discontinuities appear in the graph. The physical origin of these features lies in the **resonant field enhancement** inside the particle, where the amplitude significantly increases, leading to the excitation of a **whispering gallery mode**. In this regime, the field inside the particle forms distinct bright maxima near its boundary (see **Fig. 5(a)**). The characteristic width of these resonant cases or discontinuities is approximately $\Delta(R/\lambda) = 0.05\lambda$. These cases will now be examined in more detail.

Fig. 5 shows the near-field distribution inside the particle and the corresponding image field near the sharp resolution changing point at $R = 4.06\lambda$. The case of **minimal resolution** is illustrated in **Fig. 5(a)**, where the formal resolution reaches an extremely small value of 0.06λ at $R = 4.0575\lambda$. However, when compared to the case at $R = 4.06\lambda$, where the resolution is $d = 0.22\lambda$, the image fields appear nearly identical.

Thus, despite the particle separation differing by a factor of three, the distance between maxima in the image field remains nearly the same. This suggests that the image field does not precisely convey the geometry and spacing of the objects but rather indicates whether one or two

particles are located beneath the microsphere. Such behavior is characteristic of the excitation of **antisymmetric modes**, a phenomenon noted in [17].

In **Fig. 5(c)–(d)**, the cause of the **sharp resolution deterioration** can also be understood: it arises due to the formation of a pronounced maximum above the geometric focus. As a result, the **formal resolution condition** are no longer met, even though two distinct stripes can still be observed below this maximum.

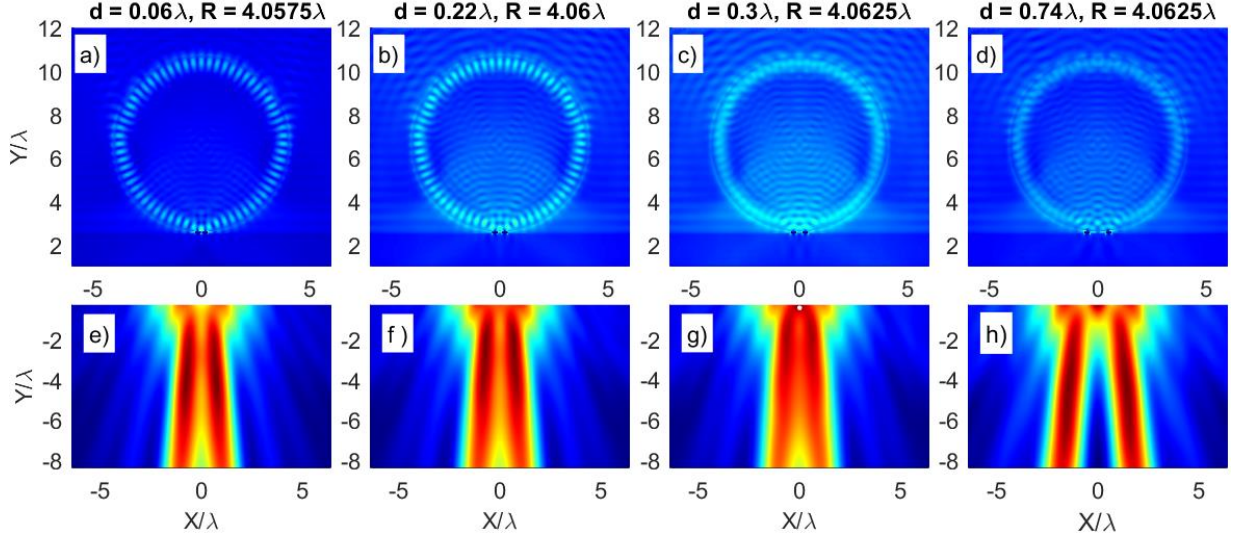


Fig. 5. Near-field distribution in reflection mode for critical scheme illumination around sharp resolution changing at $R = 4.06$. The white dot in (g) indicates the maximum field. Due to the emergence of this maximum, the optical resolution significantly **deteriorates** to 0.74. The maximum values of the near fields for (a)–(d) are related as 1:0.6:0.5:0.6. The bright stripes at the microparticle boundary in (a) indicate the excitation of a whispering gallery mode, leading to a significant enhancement of the near field.

Consider the break points on the graph in **Fig. 4(b)**. As mentioned above, the resolution at these points is undefined because the resolution condition is satisfied even at zero distance between the slits. We found such cases only in the transmission mode.

Let us examine this case in more detail using the break point at $R/\lambda = 4.4$ as an example. At first glance, it might seem that the resolution condition would continue to hold as the slit distance increases, but this is not the case. When calculated for a distance of $d = 0.1\lambda$, these conditions are no longer met, and this trend persists up to $d = 0.2\lambda$, a value that can be estimated by interpolation from the graph. Therefore, with some reservations, this value can be considered the optical resolution in this case. **Fig. 6** illustrates this behavior in more detail. This example highlights the need to develop more general criteria for defining optical image resolution in the presence of a microparticle.

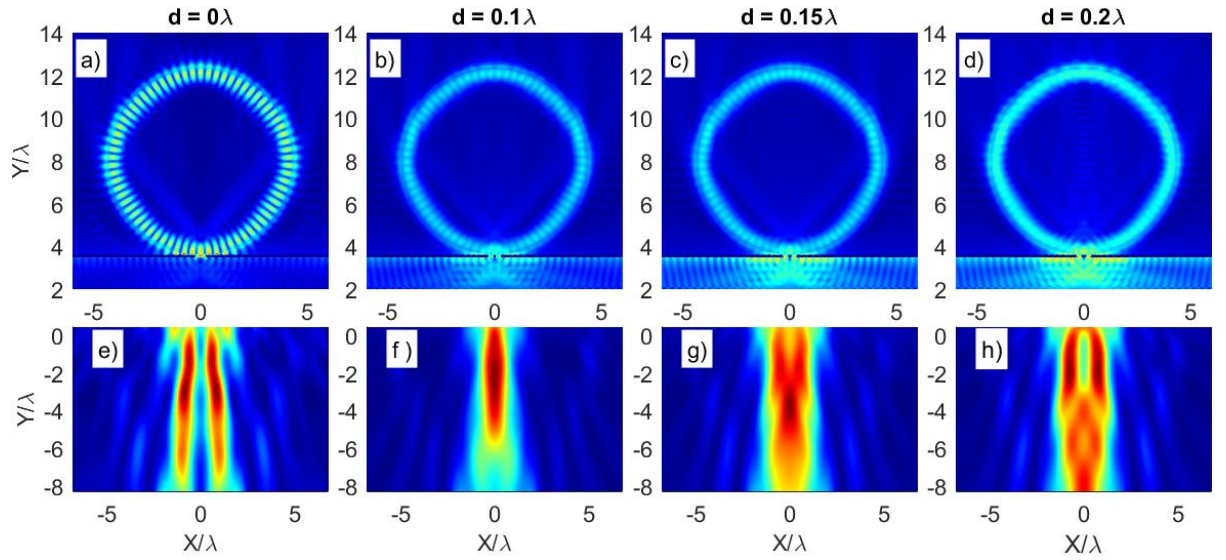


Fig. 6. (a, b, c, d) - Near-field distribution around the slits for $R = 4.4\lambda$ for critical illumination, corresponding to the break points in Fig. 4(b), with slit distances $d/\lambda = 0, 0.1, 0.2, 0.2$, respectively. (e, f, g, h) - Image fields corresponding to the cases shown in the images above. Formal conditions for distinguishability are satisfied at $d/\lambda = 0$, however, in reality, the slits are distinguishable only at $d/\lambda = 0.2$. The maximum values of the near fields for (a)–(d) are related as 1:0.4:0.3:0.3.

This enhancement of the near field leads to an increased effect of secondary illumination of the sample by the field circulating inside the particle, which in turn results in the observed features. To verify this hypothesis, we performed resolution calculations where the source was modeled as two incoherent point dipoles, represented as a uniformly distributed current within a cylinder of radius 0.025λ . The calculation geometry and model exactly match those of the reflection mode case, meaning that we **effectively** replaced the reflecting objects with point sources. In this case, local field enhancement also occurs at the mentioned points; however, it does not affect the emitted field of the source. The optical resolution remains close to the theoretical limit of 0.5λ and does not exhibit anomalies at these points, as shown in **Fig. 7**.

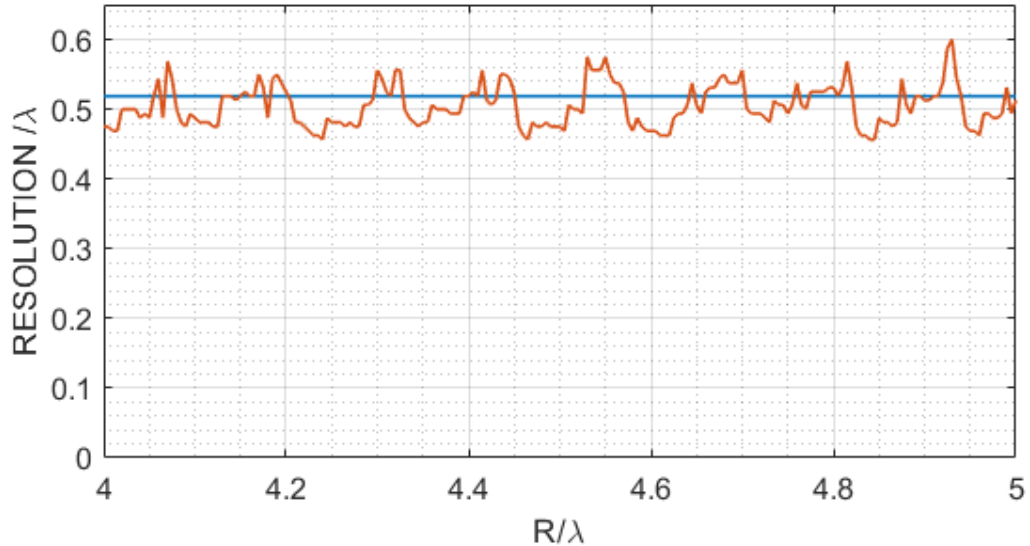


Fig. 7. The dependence of optical resolution in the point source model for free space and in the presence of a microparticle. The optical resolution in free space is 0.52λ , while in the case of a microparticle, it oscillates with a small amplitude around this value.

It should be noted that to achieve a resolution of approximately 0.5λ in the point source model, the calculation domain was extended by 10λ along the x-axis. Otherwise, the resolution

would be limited to 0.6λ . This difference is explained by the increased numerical aperture, which enhances the collection of field information. However, this extension does not affect the results for the microsphere, as most of the rays passing through the microsphere are confined within a limited cone [14]. Moreover, only the x-component of the field was used in image calculations.

A comparison of the results in **Fig. 7** for the point source model and those in **Fig. 4** for the simulation model indicates that the key factors enabling super-resolution are the interactions between radiation and the investigated sample, as was noted to some extent by Maslov [10]. This observation suggests that, in general, microspheres do not enhance optical resolution in terms of resolving individual point sources beyond the diffraction limit. A similar conclusion was drawn in our previous work, where we modeled imaging for three particles [14], as well as in our theoretical analysis of optical resolution from the perspective of the limited number of modes excited within the microsphere [12].

References

1. Z. Wang, W. Guo, L. Li, *et al.*, "Optical virtual imaging at 50 nm lateral resolution with a white-light nanoscope," *Nat. Commun.*, **2**(1), 218 (2011).
2. H. Yang, R. Trouillon, G. Huszka, *et al.*, "Super-resolution imaging of a dielectric microsphere is governed by the waist of its photonic nanojet," *Nano Lett.*, **16**(8), 4862-4870 (2016).
3. R. Boudoukha, S. Perrin, A. Demagh, *et al.*, "Near-to far-field coupling of evanescent waves by glass microspheres," *Photonics*, **8**(73), 59 (2021).
4. Y. Duan, G. Barbastathis, and B. Zhang, "Classical imaging theory of a microlens with super-resolution," *Opt. Lett.* **38**(16), 2988-2990 (2013).
5. A. Bekirov, B. Luk'yanchuk, and A. Fedyanin, "Virtual image within a transparent dielectric sphere," *JETP Lett.* **112**(6), 341-345 (2020).
6. T. Pahl, L. Hüser, S. Hagemeyer, *et al.*, "FEM-based modeling of microsphere-enhanced interferometry," *Light adv. manuf.* **3**(4), 699-711 (2022).
7. C. Simovski, and H. Reza, "A simple glass microsphere may put the end to the metamaterial superlens story," *AIP Conf. Proc.* **2300**, 020117 (2020).
8. V. Astratov, Y. Sahel, Y. Eldar, *et al.*, "Roadmap on Label-Free Super-Resolution Imaging," *Laser Photonics Rev.* **17**(12), 2200029 (2023).
9. A. Maslov, "Effect of boundary conditions in modeling of microsphere-assisted imaging," *Appl. Opt.* **63**(16) 4372-4379 (2024).
10. A. Maslov, and V. Astratov, "Origin of the super-resolution of microsphere-assisted imaging," *Appl. Phys. Lett.* **124**(6), 061105 (2024).
11. S. Lee, L. Li, Y. Ben-Aryeh, *et al.*, "Overcoming the diffraction limit induced by microsphere optical nanoscopy," *J. Opt.* **15**(12), 125710 (2013).
12. A. Bekirov, "On superresolution in virtual image in a transparent dielectric sphere," *Opt. Spectrosc.* **131**(3), 363-369 (2023).
13. A. Bekirov, B. Luk'yanchuk, Z. Wang, *et al.*, "Wave theory of virtual image," *Opt. Mater. Express* **11**(11), 3646-3655 (2021).
14. Bekirov, A. R., Wang, Z., Luk'yanchuk, B. S., & Fedyanin, A. A. (2024). Dielectric microparticles for enhanced optical imaging: an FDTD analysis of contrast and resolution. *JOSA A*, **42**(1), 45-50
15. Allen, Kenneth W., et al. "Overcoming the diffraction limit of imaging nanoplasmonic arrays by microspheres and microfibers." *Optics express* **23**.19 (2015): 24484-24496.
16. Sun W., Loeb N. G., Lin B. "Light scattering by an infinite circular cylinder immersed in an absorbing medium" *Appl. Opt.* **44**(12), 2338-2342 (2005).
17. Maslov, A. V., & Astratov, V. N. (2016). Imaging of sub-wavelength structures radiating coherently near microspheres. *Applied Physics Letters*, 108(5).